*Proceedings of the 11th Brazilian Congress of Thermal Sciences and Engineering -- ENCIT 2006*
*Braz. Soc. of Mechanical Sciences and Engineering -- ABCM, Curitiba, Brazil,- Dec. 5-8, 2006*

**Paper CIT06-0815**

# DIRECT NUMERCIAL COMPUTATION OF THE SOUND GENERATED BY TRANSONIC FLOW OVER A DEEP CAVITY

**Alexandre Gonçalves Feijó de Carvalho**
Universidade de Brasília, ENM – FT – UnB, Campus Universitário, Asa Norte, Brasília, DF, 70910-900, Brasília, DF, Brasil
alepfl@terra.com.br

**Roberto Francisco Bobenrieth Miserda**
Universidade de Brasília, ENM – FT – UnB, Campus Universitário, Asa Norte, Brasília, DF, 70910-900, Brasília, DF, Brasil
rfbm@unb.br

***Abstract.*** *The objective of this work is the direct numerical computation of the aeroacoustic far-field and near-field generated by a transonic flow over a deep cavity. The compressible Navier-Stokes equations (with no turbulence model) are numerically solved using a finite volume discretization where the fluxes are computed using the skew-symmetric form of Ducros' fourth-order numerical scheme while the time marching process is achieved using a third-order Runge-Kutta scheme proposed by Shu. Pressure coefficient data and respective phase-diagram and power spectra are obtained from the center of the cavity front wall and an analysis is made concerning the trends observed. The Reynolds number is 66,000 and the Mach number is 0.9. For this case, it is observed that the sound wave system seems to originate by the flapping motion of the shear layer interacting with the trailing edge wall, which is the possible main sound generation mechanism.*

***Keywords****. sound generation, pressure coefficient, deep cavity, transonic flow*

## 1. Introduction

Impinging shear layer are known to exhibit strong coherent oscillation associated with intense noise radiation in a wide range of applications (Rockwell, 1983). In this study, the noise radiated by a transonic flow past a two-dimensional cavity is investigated. A severe acoustic environment within and outside the cavity arises from a feedback loop, locked in by the geometry and the flow itself, as shown in many similar experimental observations (Rockwell *et al.*, 1978).

For low Mach number, the flapping shear layer crosses the cavity mouth, impinges on the back edge of the cavity, and causes an oscillating mass flow rate in the region of the cavity mouth. Sound is produced by the interaction of the shear layer with the back edge wall or by the oscillating mass flow rate in the cavity mouth region (Henderson, 2000). In this paper, it is investigated if the same mechanism is responsible for the aeroacoustic field generated in transonic flows.

The oscillations occurring in cavity flows can be categorized as fluid-dynamic, fluid-resonant, or fluid-elastic (Rockwell *et al.*, 1978). Fluid-dynamic oscillations arise from the instability of the shear layer in the cavity mouth. Fluid-resonant oscillations are the result of, or are enhanced by, resonant waves within the cavity. For shallow cavities, with depth to length ratio less than one ($D^*/L^* < 1$), transverse waves (waves traveling between the cavity floor and mouth) can be excited. Deep cavities, cavities with a depth to length ratio greater than one ($D^*/L^* > 1$), produce longitudinal waves (waves traveling between the front edge and back edge walls) (Roshko, 1954; Morse, 1999 and Rossiter, 1966). Fluid elastic resonance occurs when fluid resonance is enhanced by oscillations of the cavity surface.

The great interest in cavity flows and the large number of papers devoted to this subject stem from the wide number of applications subject to this type of flow field. These include, but are not limited to, automobile components, gas transport systems, aircraft wheel and weapon bays, and aircraft research telescope/radar cavities. In all of these applications, the designer would like to eliminate the occurrence of high pressure amplitude oscillations because they lead to unsteady loadings on components within or near the cavity or because they lead to unwanted sound.

The general noise spectrum of cavity noise contains both broadband components, introduced by the three-dimensional effects of turbulence across the shear layer, and tonal components introduced by the quasi two-dimensional flapping motion of the shear layer. In order to reduce the computational effort associated to a very well resolved computational grid, in this paper is carried out a two-dimensional simulation, although it is known that the turbulence is a three-dimensional phenomenon, and doing so, the fluctuations in the third direction are not taken into account. However, the large scale flapping motion of the shear layer, which is responsible for the low frequency tonal components can be well predicted. Broadband components on the other hand, are generated by the three-dimensional effects of turbulence and will not be predicted in a precise way with a two-dimensional unsteady flow calculation (Rubio *et al.*, 2005). On the other hand, the boundary layer prior to the separation in the cavity lip is laminar, so the transition from a laminar two-dimensional shear layer to a three-dimensional one must happen in some point over the

cavity mouth, further restricting the onset of the three-dimensional effects in the cavity, resulting in a highly transitional flow. An upstream laminar boundary layer (just ahead of the cavity) is imposed in this work since it was observed experimentally (Krishnamurty, 1956) that an initially laminar shear layer tends to produce a more intense sound field when compared to the sound field associated to an initially turbulent shear layer because in the former case the resulting flapping motion of the shear layer is quasi two-dimensional. The classical work of Rossiter (1966) pointed out that even for three-dimensional subsonic and transonic cavities the fundamental behavior, particularly along the cavity centerline, appears to be predominantly two-dimensional. Rizzetta (1988) carried out numerical studies over a three-dimensional cavity at a Mach number of 1.5 and also came with the same conclusion, i.e., the fundamental behavior of the unsteady phenomena is two-dimensional. The overview paper of Grace (2001) points out various works where a two-dimensional simulation is performed in order to predict the aeroacoustic field in subsonic, transonic and supersonic cavities at high Reynolds number.

The geometrical parameters of the cavity are based on the benchmark problem for category 6 of the Third Computational Aeroacoustics (CAA) Workshop on Benchmark Problems, organized by the National Aeronautics and Space Administration (NASA), held in 2000. This benchmark is intended for automotive door gap problems, associated to low Mach numbers. In this paper, the geometry of this benchmark is used to analyze aeronautic door gap problems in the transonic range. The Mach number is 0.9 and the Reynolds number is 66,000. The numerical code implemented by Bobenrieth Miserda and Mendonça (2005), used in the present simulation, solves the compressible Navier-Stokes equations (with no turbulence model) through a finite volume discretization, where the fluxes are computed using the skew-symmetric form of Ducros' fourth-order numerical scheme (Ducros *et al.*, 2000) while the time marching process is achieved using a third-order Runge-Kutta scheme proposed by Shu (Yee, 1997).

## 2. Methodology

In this work, a Direct Noise Computation (DNC), based on the solution of the two-dimensional compressible Navier-Stokes equations, with no turbulence model, is performed. The nondimensional form of the Navier-Stokes equations can be written as:

$$\frac{\partial \rho}{\partial t} + \frac{\partial}{\partial x_i}(\rho u_i) = 0\,, \tag{1}$$

$$\frac{\partial}{\partial t}(\rho u_i) + \frac{\partial}{\partial x_j}(\rho u_i u_j) = -\frac{\partial p}{\partial x_i} + \frac{\partial \tau_{ij}}{\partial x_j}\,, \tag{2}$$

$$\frac{\partial}{\partial t}(\rho e_T) + \frac{\partial}{\partial x_i}(\rho e_T u_i) = -\frac{\partial}{\partial x_i}(p u_i) + \frac{\partial}{\partial x_i}(\tau_{ij} u_j) - \frac{\partial q_{x_i}}{\partial x_i}\,. \tag{3}$$

All the variables are in nondimensional form and have their usual meaning, i.e., $\rho$ is the density, $t$ is the temporal coordinate, $x_i$ is the $i$-direction spatial coordinate, $u_i$ is the $i$-direction component of the velocity vector, $p$ is the pressure, $\tau_{ij}$ denotes the viscous stress tensor, $e_T$ is the total energy per unit of mass and $q_{xi}$ is the heat-flow density in the $i$-direction.

The nondimensional form of the flow variables and properties are defined as

$$x_i = \frac{x_i^*}{b^*},\quad u_i = \frac{u_i^*}{U_\infty^*},\quad t = \frac{t^*}{b^*/U_\infty^*},\quad p = \frac{p^*}{\rho_\infty^*\left(U_\infty^*\right)^2},\quad \rho = \frac{\rho^*}{\rho_\infty^*},\quad e_T = \frac{e_T^*}{\left(U_\infty^*\right)^2} \tag{4}$$

$$\mu = \frac{\mu^*}{\mu_\infty^*},\quad e = \frac{e^*}{\left(U_\infty^*\right)^2},\quad e_k = \frac{e_k^*}{\left(U_\infty^*\right)^2},\quad c_v = \left[\frac{T_\infty^*}{\left(U_\infty^*\right)^2}\right] c_v^*,\quad T = \frac{T^*}{T_\infty^*}, \tag{5}$$

where the asterisk denotes dimensional quantities, $b^*$ is the width of the overhang at the cavity entrance Fig. (1), $\mu^*$ is the dynamic viscosity and $T^*$ is the temperature. $U^*_\infty$, $T^*_\infty$, $\rho^*_\infty$ and $\mu^*_\infty$ are, respectively, the velocity, temperature, density and dynamic viscosity of the undisturbed flow.

The nondimensional viscous stress tensor is given by

$$\tau_{ij} = \frac{1}{\mathrm{Re}}\left(\mu S_{ij}\right) = \frac{1}{\mathrm{Re}}\left\{\mu\left[\left(\frac{\partial u_i}{\partial x_j} + \frac{\partial u_j}{\partial x_i}\right) - \frac{2}{3}\delta_{ij}\frac{\partial u_k}{\partial x_k}\right]\right\}, \tag{6}$$

where $\delta_{ij}$ is the Kronecker delta. The Reynolds number is defined as

$$\mathrm{Re} = \frac{\rho_\infty^* U_\infty^* b^*}{\mu_\infty^*}. \tag{7}$$

Defining $e$ as the nondimensional internal energy per unit of mass, $e_k$ as the nondimensional kinetic energy per unit of mass and $c_v$ as the nondimensional specific heat at constant volume, the total energy is given by the sum of the internal and kinetic specific energy as

$$e_T = e + e_k = c_v T + \frac{u_i u_i}{2} \tag{8}$$

and the nondimensional heat-flux density is

$$q_{x_i} = -\frac{\mu}{(\gamma-1)M^2\,\mathrm{Re}\,\mathrm{Pr}}\left(\frac{\partial T}{\partial x_i}\right), \tag{9}$$

where the $M$ and Pr are the Mach and the Prandtl numbers, respectively, and are defined as

$$M = \frac{U_\infty^*}{\sqrt{\gamma R^* T_\infty^*}}, \qquad \mathrm{Pr} = \frac{c_p^*}{k_\infty^*}\mu_\infty^*, \tag{10}$$

where $\gamma$ is the specific heat ratio, $R^*$ is the specific gas constant, $c_p{}^*$ is the specific heat at constant pressure and $k_\infty{}^*$ is the thermal conductivity of the undisturbed flow.

In this work, the Prandtl number is considered a constant with the value $\mathrm{Pr} = 0.72$. For a thermally and calorically perfect gas, the nondimensional equation of state can be written as

$$p = (\gamma-1)\rho e \tag{11}$$

and

$$T = \frac{\gamma M^2 p}{\rho}. \tag{12}$$

The nondimensional molecular viscosity is obtained using the Sutherland's formula, where $C_1$ and $C_2$ are the nondimensional first and second gas constants,

$$\mu = C_1\frac{T^{3/2}}{T + C_2}, \qquad C_1 = \left[\frac{\left(T_\infty^*\right)^{1/2}}{\mu_\infty^*}\right]C_1^*, \qquad C_2 = \frac{C_2^*}{T_\infty^*}. \tag{13}$$

The boundary conditions at the walls of the two-dimensional cavity and at the downstream surface are a no-slip condition for the velocity field, an adiabatic wall for the temperature field and a null gradient in the normal direction at the wall for the pressure field. The boundary condition for the upstream surface is a slip condition till the beginning of the cavity overhang in order to develop an appropriate boundary layer thickness for the present case. The adiabatic wall and null pressure gradient in the normal wall direction are also applied for the latter surface.

Since the geometry of interest is a two-dimensional cavity, the two-dimensional form of the Navier-Stokes equations is used. In order to numerically solve this equations using a finite volume approach, Eqs. (1), (2) and (3) are written in the following vector form (Anderson, 1983):

$$\frac{\partial \mathbf{U}}{\partial t} + \frac{\partial \mathbf{E}}{\partial x} + \frac{\partial \mathbf{F}}{\partial y} = 0, \tag{14}$$

where **U** is the nondimensional conservative-variables vector, **E** and **F** are the nondimensional flux vectors. These vectors are given by

$$\mathbf{U}=\begin{bmatrix}\rho\\ \rho u\\ \rho v\\ \rho e_T\end{bmatrix},\quad \mathbf{E}=\begin{bmatrix}\rho u\\ \rho u^2+p-\tau_{xx}\\ \rho uv-\tau_{xy}\\ (\rho e_T+p)u-u\tau_{xx}-v\tau_{xy}+q_x\end{bmatrix},\quad \mathbf{F}=\begin{bmatrix}\rho v\\ \rho vu-\tau_{xy}\\ \rho v^2+p-\tau_{yy}\\ (\rho e_T+p)v-u\tau_{xy}-v\tau_{yy}+q_y\end{bmatrix}, \tag{15}$$

where *u* and *v* are, respectively, the nondimensional component of the velocity vector in the *x*-direction and *y*-direction.

Defining the flux tensor $\Pi$ as

$$\Pi=\mathbf{E}\otimes\mathbf{i}+\mathbf{F}\otimes\mathbf{j}, \tag{16}$$

where **i** and **j** are unit vectors in the *x*-direction and *y*-direction. Eq. (14) can be rewritten as

$$\frac{\partial\mathbf{U}}{\partial t}+\nabla\cdot\Pi=0, \tag{17}$$

Integrating the above equation over the control volume *V*, and applying the divergence theorem to the first term of right-hand side results

$$\frac{\partial}{\partial t}\int_V\mathbf{U}\,dV=-\int_V(\nabla\cdot\Pi)\,dV=-\int_S(\Pi\cdot\mathbf{n})\,dS\cdot \tag{18}$$

The volumetric mean of vectors **U** in the control volume *V* is defined as

$$\bar{\mathbf{U}}\equiv\frac{1}{V}\int_V\mathbf{U}\,dV, \tag{19}$$

where the upper bar means volumetric mean of the variable. Eq. (18) is written as

$$\frac{\partial\bar{\mathbf{U}}}{\partial t}=-\frac{1}{V}\int_S(\Pi\cdot\mathbf{n})\,dS\cdot \tag{20}$$

For the volume $(i,j)$, the first-order approximation of the temporal derivative is given by

$$\left(\frac{\partial\overline{\mathbf{U}}}{\partial t}\right)_{i,j}=\frac{\Delta\overline{\mathbf{U}}_{i,j}}{\Delta t}+O(\Delta t), \tag{21}$$

and the temporal approximation of Eq. (20) for a quadrilateral and two-dimensional control volume is

$$\Delta\,\bar{\mathbf{U}}_{i,j}=-\frac{\Delta t}{V_{i,j}}\left[\int_{S_{i+1/2}}(\Pi\cdot\mathbf{n})\,dS+\int_{S_{i-1/2}}(\Pi\cdot\mathbf{n})\,dS+\int_{S_{j+1/2}}(\Pi\cdot\mathbf{n})\,dS+\int_{S_{j-1/2}}(\Pi\cdot\mathbf{n})\,dS\right], \tag{22}$$

where $S_{i+1/2}$ is the common surface between volume $(i,j)$ and volume $(i+1,j)$, **n** is the normal unit vector and $\Delta t$ is the nondimensional time step. Defining

$$\mathcal{F}\left(\overline{\mathbf{U}}\right)_{i,j}=(\Pi\cdot\mathbf{S})_{i+1/2}+(\Pi\cdot\mathbf{S})_{i-1/2}+(\Pi\cdot\mathbf{S})_{j+1/2}+(\Pi\cdot\mathbf{S})_{j-1/2}, \tag{23}$$

the spatial approximation of Eq. (22) is

$$\Delta\overline{\mathbf{U}}_{i,j}=-\frac{\Delta t}{V_{i,j}}\left[\mathcal{F}\left(\overline{\mathbf{U}}\right)_{i,j}-\mathcal{D}\left(\overline{\mathbf{U}}\right)_{i,j}\right], \tag{24}$$

where $\mathcal{D}\left(\overline{\mathbf{U}}\right)_{i,j}$ is an artificial dissipation. It is important to note that Eq. (24) is a spatial approximation of Eq. (22) because the tensor $\Pi$ is considered constant over each of the four control surfaces that define the control volume.

In order to calculate $\mathcal{F}\left(\overline{\mathbf{U}}\right)_{i,j}$, the flux of tensor $\Pi$ trough the control surfaces must be calculated. The explicit form of this calculation as well as the implementation of the artificial dissipation, $\mathcal{D}\left(\overline{\mathbf{U}}\right)_{i,j}$, is given by Bobenrieth Miserda and Mendonça (2005).

In order to advance Eq. (24) in time, a third-order Runge-Kutta is used as proposed by Shu (Yee, 1997). This yield to

$$\overline{\mathbf{U}}^{1} = \overline{\mathbf{U}}^{n} - \frac{\Delta t}{V_{i,j}}\left[\boldsymbol{\mathcal{F}}\left(\overline{\mathbf{U}}^{n}\right) - \boldsymbol{\mathcal{D}}\left(\overline{\mathbf{U}}^{n}\right)\right], \tag{25}$$

$$\overline{\mathbf{U}}^{2} = \frac{3}{4}\overline{\mathbf{U}}^{n} + \frac{1}{4}\overline{\mathbf{U}}^{1} - \frac{1}{4}\left\{\frac{\Delta t}{V_{i,j}}\left[\boldsymbol{\mathcal{F}}\left(\overline{\mathbf{U}}^{1}\right) - \boldsymbol{\mathcal{D}}\left(\overline{\mathbf{U}}^{1}\right)\right]\right\}, \tag{26}$$

$$\overline{\mathbf{U}}^{n+1} = \frac{1}{3}\overline{\mathbf{U}}^{n} + \frac{2}{3}\overline{\mathbf{U}}^{2} - \frac{2}{3}\left\{\frac{\Delta t}{V_{i,j}}\left[\boldsymbol{\mathcal{F}}\left(\overline{\mathbf{U}}^{2}\right) - \boldsymbol{\mathcal{D}}\left(\overline{\mathbf{U}}^{2}\right)\right]\right\}. \tag{27}$$

As used in this work, the numerical method is fourth-order accurate in space and third-order accurate in time.

## 3. Numerical Specifications

### 3.1. Cavity Geometry

The geometry used from the category 6 problem (Henderson, 2000) is showed in Fig. (1).

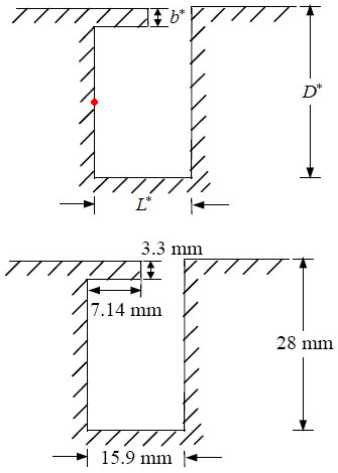


Figure 1. Cavity geometry.

The red point at the center of the left cavity wall indicates the location where $c_p$ data as a function of time is obtained.

### 3.2. Computational Grid

A portion of the computational mesh is displayed in Fig. (2). The total mesh is compounded by one non-uniform Cartesian grid outside the cavity and two uniform Cartesian grid inside the cavity in order to provide the cavity overhang, as required from the category 6 problem (Henderson, 2000).

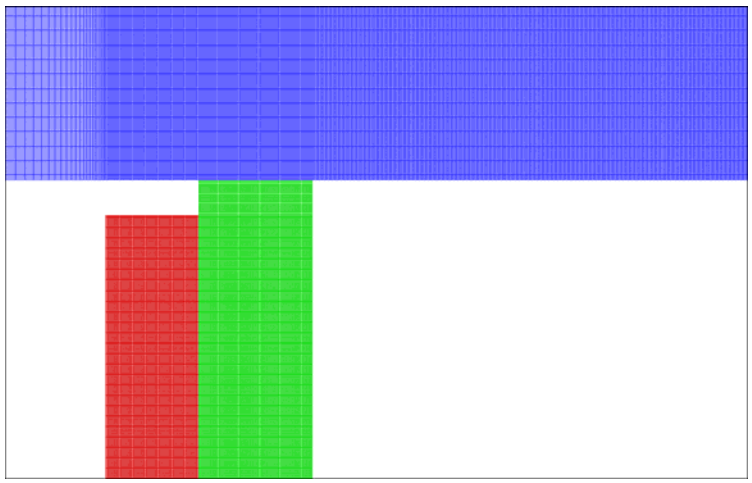

Figure 2. Portion of the cavity Mesh. The outside cavity grid (blue) has 1050 × 975 volumes; the grid below the cavity overhang (red) has 72 ×228 volumes and the last one (green) has 90 ×255 volumes.

The computational domain extends $343\,b^*$ downstream and $228\,b^*$ in the normal direction.

## 4. Results

### 4.1. Far-Field Results

Figure (3) displays a visualization based on the magnitude of the gradients of nondimensional temperature showing the structures of the radiated field. This type of visualization is used since the aeroacoustic phenomenon studied involves the interaction of boundary and shear layers, vortex structures, pressure and shock waves. The gradients of the nondimensional temperature field are very sensitive to all the aforementioned flow features, facilitating their joint presentation. It is possible to observe two types of pressure wave patterns, being the first one originated from the interaction of the flapping shear layer with the cavity lip (at the separation point) and the second one resulting from the interaction of the flapping shear layer with the back edge of the cavity (at the reattachment point).

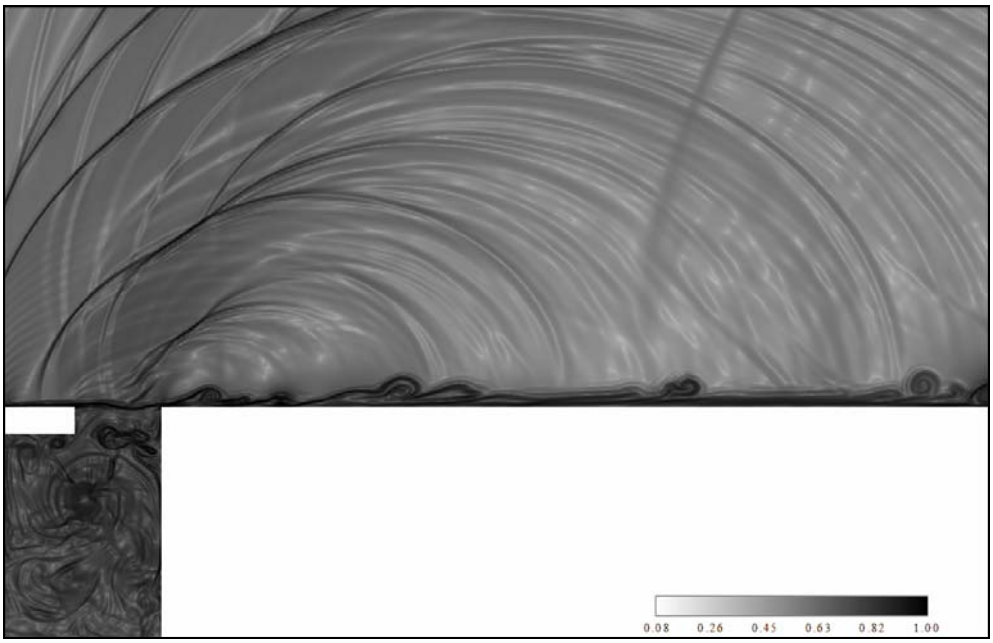


Figure 3. Far-field visualization of the two wave patterns based on gradients of nondimensional temperature.

Also it is noted from Fig. (3) the sound waves production from the collision between vortices along the downstream boundary layer.

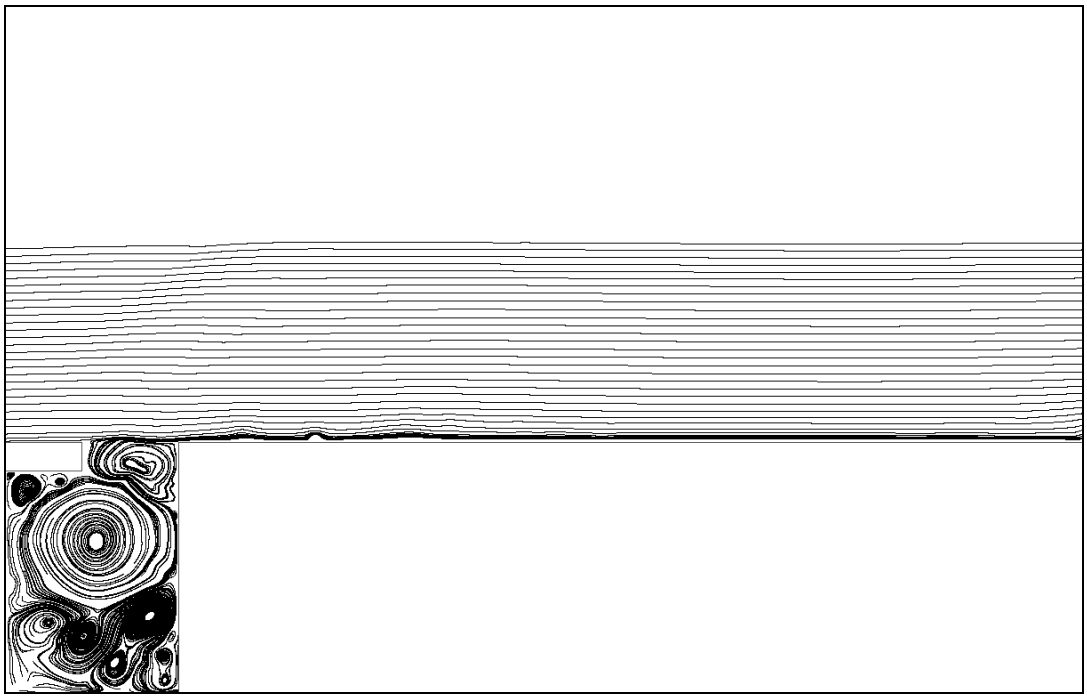

Figure 4. Far-field visualization of the two wave patterns based on mean streamlines.

Figure (4) shows the mean streamlines from the same visualization of Fig. (3). It is noted that the streamlines along the cavity mouth are nearly horizontal and a main vortex dominates half the cavity region. Figure (5) displays a low pressure region just in the centre of the main vortex and this region appears to be the result of the vortical swirling motion in the cavity. At the impingement region (rear edge of the cavity), $C_p$ reaches its higher value about 0.6. These qualitative flow features is very similar to those presented by Rowley *et al.* (2002) concerning the shear-layer mode of oscillation which is characterized by a feedback process: the roll-up of vorticity in the shear layer, impingement and scattering of acoustics waves at the downstream cavity edge, upstream acoustic wave propagation, and receptivity of the shear layer to acoustic disturbances.

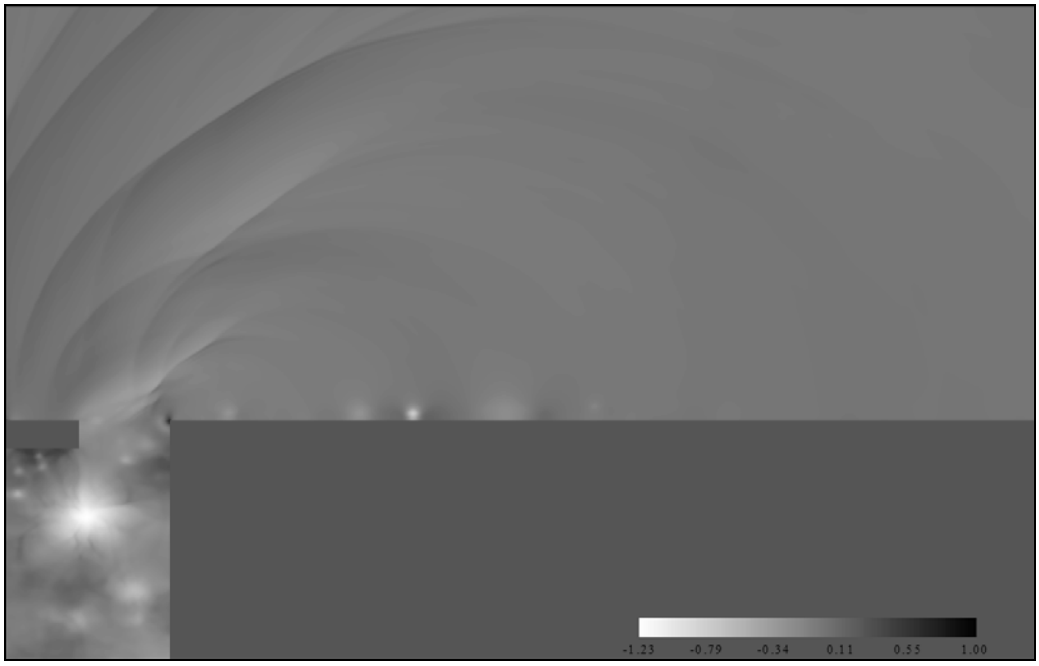


Figure 5. Far-field visualization based on contours of $C_p$.

**4.2. Near-Field Results**

The near field is now investigated to identify the noise generation mechanism, and in particular to determine the origin of the two wave patterns observed previously in Fig (3). Figure (6) presents the cycling mechanism of the flapping shear layer crossing the cavity mouth and a vortex structure inside it. It is observed a dominant vortex structure inside the cavity that presents a circular movement around the cavity centre and generates radial waves that are reflected longitudinally between the cavity walls. The vortex inside the shear layer is shed from its front edge separation and travels downstream, growing with convection (Fig. (6), (a) and (b)). As it impinges on the back edge, the shear layer vortex centre is clipped on this edge (Fig. (6), (c)). Part of the vortex spills over the cavity and is convected downstream, increasing the thickness of the reattached boundary layer. The other component is swept downward into the cavity creating recirculating regions. Figure (6), (d) shows the restart of the shear layer vortex formation. As the vortex shedding at the front edge wall and the clipping of its centre on the back edge wall occur, the two far-field wave patterns seem in Fig. (3) are formed by consequence.

A portion of the signal of the unsteady pressure coefficient is shown is Fig. (7) as well as its mean. It is worth noting that this mean has a cumulative nature, resulting in a value that stabilizes with time. The flow inside the cavity has a self-sustained oscillatory nature but is still irregular. This unsteady flow behavior inside the cavity appears to be driven by the main vortex structure generating the radial waves which may be the main responsible for the pressure oscillations. However, the mean value of $c_p$ stabilizes after a time of about $858 b^* / U_\infty$.

From the phase-diagram displayed in Fig. (8) there is a non-periodic behavior of the pressure field within the cavity possibly due to the random formation of small vortex structures and the dynamics of generation of radial waves from the main vortex structure, that are reflected longitudinally between the cavity walls. The overall power spectra indicates two major peaks at $St = 0.125$ and $St = 0.130$, which the former seems to correspond to the impingement frequency of the radial waves on the cavity left wall and the latter seems to be related to the frequency of the circular movement of the main vortex inside the cavity, approaching and distancing from the cavity left wall.

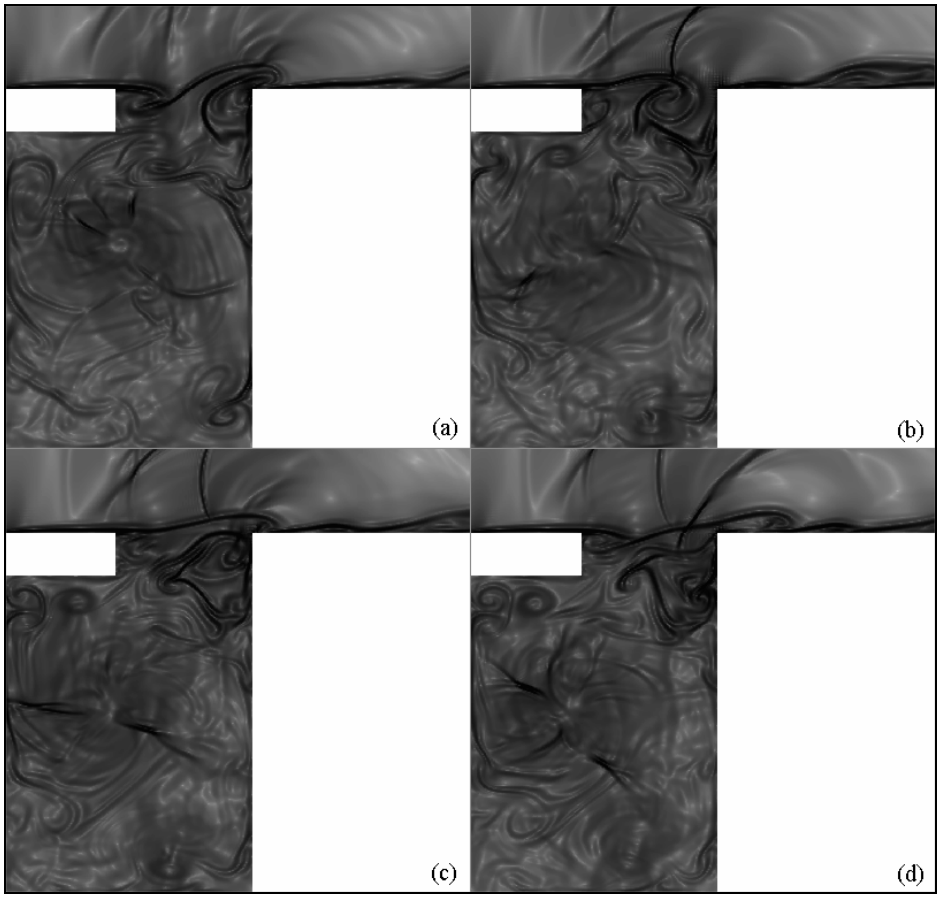


Figure 6. Near-field visualizations based on gradients of nondimensional temperature displaying the main vortex and its generated radial waves inside the cavity and the interaction between the shear layer and the leading edge and trailing edge cavity walls. White corresponds to 0 and black corresponds to 1.

Several secondary peaks are observed at $St = 0.146$, $St = 0.158$ and $St = 0.180$ which could be related to several types of wave frequency propagation caused by small vortex structures formed inside the cavity.

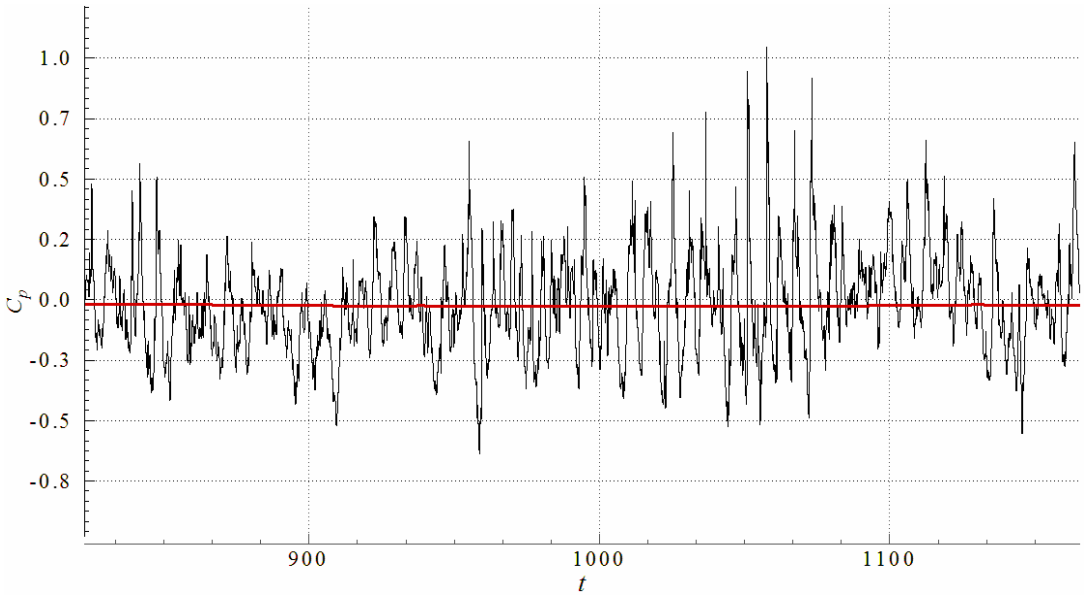


Figure 7. Unsteady (black) and mean (red) pressure coefficient as a function of nondimensional time extracted from the point located at the center of the cavity left wall.

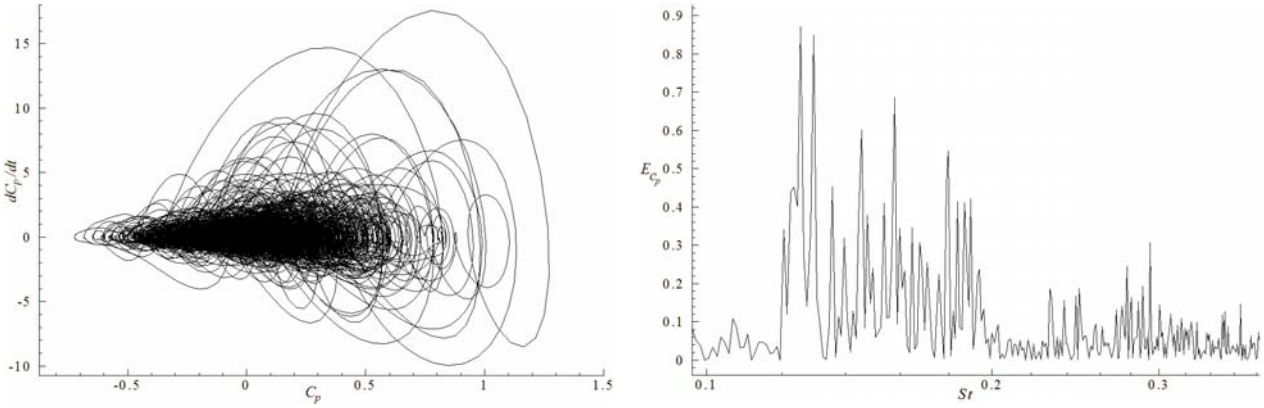


Figure 8. Phase-diagram and power spectra as a function of the Strouhal number, $St = f^* L^* / U_\infty^*$, derived from the $c_p$ data as a function of time.

## 5. Conclusion

A direct calculation of the sound radiated by a flow over a 2-D deep cavity is carried out. This methodology was implemented in order to asset the effects of the shear layer impingement on the back edge wall of the cavity as the possible main responsible for the noise generation mechanism concerning the aeroacoustic far-field. Although it was carried out a 2D simulation, this approach is capable to provide all the necessary interactions between the flow and acoustics, proving to be a powerful tool to determine the noise generation mechanism. The far field dynamics of the wave sound formation are very similar to those observed by Rowley *et al.* (2002) concerning the shear-layer mode of oscillation which is characterized by a feedback process. It was observed inside the cavity a formation of small vortex structures and a main one that generates radial waves which are reflected longitudinally between the cavity walls. These waves' reflections confirm their longitudinal pattern inherent from cavities with a depth to length ratio greater than one ($D^* / L^* > 1$) (Roshko, 1954; Morse, 1999 and Rossiter, 1966). The phase-diagram presented in Fig. (8) indicates an non-periodic pressure field behavior inside the cavity and the correspondent power spectra shows that the greatest part of the energy is concentrated in two peaks that seems to be related to the impingement frequency of the radial waves on

the cavity front wall and to the frequency of the circular movement of the main vortex inside the cavity, approaching and distancing from the cavity front wall.

## 6. References

Anderson, D. A., Tannehill, J. C. and Pletcher, R. H., 1983, "Computational Fluid Mechanics and Heat Transfer", Hemisphe Publishing Corporation, New York.

Bobenrieth Miserda, R. F., Mendonça, A. F. de, 2005, "Numerical Simulation of the Vortex-Shock Interactions in a Near-Base Laminar Flow", AIAA 43rd Aerospace Sciences Meeting and Exhibit, AIAA 2005-0316, Reno, Nevada.

Ducros, F., Laporte, F., Soulères, T., Guinot, V., Moinat, P. and Caruelle, B., 2000, "High-Order Fluxes for Conservative Skew-Symmetric-like Schemes in Structured Meshes: Application to Compressible Flows", Journal of Computational Physics, Vol. 161, pp. 114-139.

Grace, S. M., 2001, "An Overview of Computational Aeroacoustic Techniques Applied to Cavity Noise Prediction", 39th AIAA Aerospace Sciences Meeting and Exhibit, Reno, NV.

Henderson, B., 2000, "Automobile Noise Involving Feedback Sound Generation by Low Speed Cavity Flows", Third Computational Aeroacoustics (CAA) Workshop on Benchmark Problems, NASA, pp. 95-100.

Kryshnamurty, K., 1956, "Sound Radiation from Surface Cutouts in High Speed Flow", California Institute of Technology, Pasadena, California.

Morse, P., and Shieh, C., 1999, "Parallel Numerical Simulation of Subsonic Cavity Noise", AIAA paper 99-1891.

Rizzetta, D. P., 1988, "Numerical Simulation of Supersonic Flow over a Three-Dimensional Cavity", AIAA Journal, Vol 26, No 7.

Rockwell, D., and Naudasher, E., 1978, "Review – Self-sustaining Oscillation of Flow Past Cavities", Transactions of ASME, pp. 152-165.

Rockwell, D, 1983, "Oscillations of Impinging Shear Layers", AIAA Journal 21, pp. 152-165.

Roshko, A., 1954, "Some Measurements of the Flow in a Rectangular Cutout", NACA NAW-6296.

Rossiter, J.E., 1966 "Wind Tunnel Experiments on the Flow Over Rectangular Cavities at Subsonic and Transonic Speeds", Aeronautical Research Council Reports and Memorandum No. 3438.

Rowley, C.W., Colonius, T., Basu, A. J. 2002 "On Self-Sustained Oscillation in Two-Dimensional Compressible Flow Over Rectangular Cavities", Journal of Fluid Mechanics, vol. 455, pp. 315-346.

Rubio, G., Roeck, W., Baelmans, M., Desmet, W., 2005 "Numerical Study of Noise Generation Mechanism in Rectangular Cavities", Euromech Colloquium 467: Turbulent and Noise Generation, July 18-20, Marseille, France.

Yee, H. C., 1997, "Explicit and Implicit Multidimensional Compact High-Resolution Shock-Capturing Methods: Formulation," Journal of Computational Physics, Vol. 131, pp. 216, 232